ISTANBUL TECHNICAL UNIVERSITY ★ FACULTY OF AERONAUTICS AND ASTRONAUTICS

COMPUTATIONAL FLUID DYNAMICS ANALYSIS OF NASA ROTOR 37 USING OPEN SOURCE SOFTWARE

GRADUATION PROJECT

Halit OKUMUŞ

Department of Aeronautical Engineering

Thesis Advisor: Prof. Dr. Fırat Oğuz EDİS

AUGUST 2021

ISTANBUL TECHNICAL UNIVERSITY ★ FACULTY OF AERONAUTICS AND ASTRONAUTICS

COMPUTATIONAL FLUID DYNAMICS ANALYSIS OF NASA ROTOR 37 USING OPEN SOURCE SOFTWARE

GRADUATION PROJECT

Halit OKUMUŞ

(110120276)

Department of Aeronautical Engineering

Thesis Advisor: Prof. Dr. Fırat Oğuz EDİS

20 AUGUST 2021

İSTANBUL TEKNİK ÜNİVERSİTESİ ★ UÇAK VE UZAY BİLİMLERİ FAKÜLTESİ

NASA ROTOR 37 BIÇAĞININ AÇIK KAYNAK KODLU YAZILIM KULLANILARAK HESAPLAMALI AKIŞKAN DİNAMİĞİ ANALİZİ

BİTİRME ÇALIŞMASI

Halit OKUMUŞ

(110120276)

Uçak Mühendisliği Bölümü

Tez Danışmanı: Prof. Dr. Fırat Oğuz EDİS

20 AĞUSTOS 2021

iv

Halit OKUMUŞ, student of ITU Faculty of Aeronautics and Astronautics student ID 110120276, successfully defended the **graduation** entitled "**COMPUTATIONAL FLUID DYNAMICS ANALYSIS OF NASA ROTOR 37 USING OPEN SOURCE SOFTWARE**", which he prepared after fulfilling the requirements specified in the associated legislations, before the jury whose signatures are below.

Thesis Advisor :   **Prof. Dr. Fırat Oğuz EDİS**   ....
                        İstanbul Technical University

Jury Members :   **Assoc. Prof. Bayram ÇELİK**   ....
                        İstanbul Technical University

                        Prof. Dr. Aydın MISIRLIOĞLU   ....
                        İstanbul Technical University

Date of Submission : 20 August 2021

Date of Defense :   26 August 2021

To my family,

FOREWORD

In the study titled "Computational Fluid Dynamics Analysis of Nasa Rotor 37 Using Open Source Software", analysis of Rotor 37 was performed using OpenFOAM software.

I would like to thank my advisor Prof. Dr. Fırat Oğuz EDİS for his support and contributions in the realization of this study.

As in all areas of my life, I would like to thank my family, especially my dear mother and father, who stood by me at every stage while preparing my thesis.

August 2021   Halit OKUMUŞ

x

TABLE OF CONTENTS

ABBREVIATIONS

CFD   **:** Computational Fluid Dynamics
NASA   **:** National Aeronautics and Space Administration
OpenFOAM **:** Open-source Field Operation and Manipulation
IGV   **:** Inlet Guide Vanes
EGV   **:** Exit Guide Vanes
NA   **:** No Answer
PS   **:** Pressure Side
SS   **:** Suction Side
RANS   **:** Reynolds-Averaged Navier-Stokes
3D   **:** Three-dimensional
CAD   **:** Computer-aided Design
LE   **:** Leading Edge
TE   **:** Trailing Edge
R37   **:** NASA Rotor 37
MRF   **:** Multi Reference Frame
SIMPLE   **:** Semi-implicit Method for Pressure Linked Equations

SYMBOLS

ρ	**:** Density
∇	**:** Gradient
V	**:** Velocity
p	**:** Pressure
f	**:** Body force
τ	**:** Shear stress
u	**:** Velocity component in x-direction
v	**:** Velocity component in y-direction
w	**:** Velocity component in z-direction
e	**:** Internal energy
$\dot{q}$	**:** Heat transfer rate per unit mass
T	**:** Temperature
k	**:** Turbulent kinetic energy
ε	**:** Turbulent kinetic energy dissipation rate
μ_t	**:** Turbulent viscosity

SUBSCRIPTS

xy	**:** x-y plane
xz	**:** x-z plane
yz	**:** y-z plane

LIST OF TABLES

LIST OF FIGURES

COMPUTATIONAL FLUID DYNAMICS ANALYSIS OF NASA ROTOR 37 USING OPEN SOURCE SOFTWARE

SUMMARY

CFD is used to solve many engineering problems with complex flows. In this thesis, Rotor 37 developed by NASA was preferred for flow analysis. NASA Rotor 37 is an axial compressor with transonic flow.

Open-source software, OpenFOAM v9, was preferred for the analysis of Rotor 37. Analysis of the passage consisting of only one blade of Rotor 37, which has 36 blades, has been made, thus saving computational cost and time. For the computational domain, a hexandral mesh was created using ANSYS TurboGrid 19.2 software. The cyclicAMI boundary condition is used for the periodic surfaces of the generated computational domain. In the analysis, rhoSimpleFoam solver and k-epsilon turbulence model were used with MRF approach.

The results obtained in the study were compared with the experimental data obtained by NASA. For comparison, the variation of the total pressure and total temperature ratios of the compressor from the hub to the tip is examined. In addition, slices were taken from the distances of 20%, 51% and 80% span from hub and the relative Mach number, total pressure ratio and total temperature ratio were shown. The differences in the results obtained from the experimental data could be due to the poor mesh quality of the domain, especially at the blade leading and trailing edges.

NASA ROTOR 37 BIÇAĞININ AÇIK KAYNAK KODLU YAZILIM KULLANILARAK HESAPLAMALI AKIŞKAN DİNAMİĞİ ANALİZİ

ÖZET

CFD karmaşık akışa sahip bir çok mühendislik problemini çözebilmek için kullanılır. Bu tezde akış analizi için NASA tarafından geliştirilen Rotor 37 bıçağı tercih edildi. NASA Rotor 37 transonik akışa sahip eksenel bir kompresördür.

Rotor 37'nin analizi için açık kaynak kodlu yazılım olan OpenFOAM v9 tercih edilmiştir. 36 bıçağa sahip olan Rotor 37'nin sadece tek bir bıçağından oluşan geçitin analizi yapılmış ve bu sayede hesaplama maliyetinden ve zamandan tasarruf edilmiştir. Hesaplama alanı için ANSYS TurboGrid 19.2 yazılımı kullanılarak hexandral örgü ağı oluşturulmuştur. Oluşturulan hesaplama alanının periyodik yüzeyleri için cyclicAMI sınır koşulu kullanılmıştır. Analizde çözücü olarak rhoSimpleFoam ve k-epsilon türbülans modeli MRF yaklaşımı ile kullanılmıştır.

Çalışmada elde edilen sonuçlar NASA tarafından elde edilmiş deneysel verilerle karşılaştırılmıştır. Karşılaştırma için kompresörün toplam basınç ve toplam sıcaklık oranlarının merkezden uç kısıma doğru değişimi incelenmiştir. Ayrıca, merkezden %20, %51 ve %80 uzunluktaki mesafelerden kesitler alınarak göreceli Mach sayısı, toplam basınç oranı ve toplam sıcaklık oranı gösterilmiştir. Elde edilen sonuçların deneysel verilerden farklı olması özellikle bıçak uçlarındaki kalitesiz örgü yapısından kaynaklanıyor olabilir.

1 INTRODUCTION

The development of the Navier-Stokes equations, which is the milestone of scientific studies carried out up to the present, in order to understand the nature of fluids has made it possible to analyze all flows successfully. Although it is possible to solve simple flow problems analytically using Navier-Stokes equations, numerical methods should be used to solve complex flow problems today.

Computational Fluid Dynamics (CFD) is a branch that analyzes and solves problems by numerically solving differential equations governing the transport of mass, momentum, turbulent variables and energy. [1] Thanks to modern computers with powerful computational capacity, necessary flow calculations are made using various software to simulate the interaction of gases and liquids with surfaces defined by boundary conditions in many fields such as aviation, architecture, automotive, biomedical and electronics. [2] In this thesis, compressible flow analysis of NASA Rotor 37 blade was performed using OpenFOAM software.

The development of CFD software for commercial use began when NASA and Boeing publicly released the codes in the 1980s. CHAM's software, PHOENICS, was the first commercial CFD software released in 1981. [3] Today, there are commercial CFD software such as ANSYS, STAR-CCM, AVL-FIRE, and PHOENICS, as well as open source CFD software such as SimFlow and OpenFOAM. In this thesis, OpenFOAM was chosen because of its open source code and strong computational capacity.

A turbomachine is any device that collects energy from or imparts energy to a constantly flowing stream of fluid. A turbomachine, to clarify, is a power or heat generating machine that uses the dynamic action of a rotating element, the rotor, to modify the energy level of a continuously flowing fluid through the machine. [4] The general classification of turbomachines is made in three different ways. The first of these is made according to the functions of the turbomachine, the second according to the nature of the working environment and the last according to the flow direction. According to their function, turbomachines are devices that generate or absorb work.

Compressors are turbomachines that absorb work, while turbines are turbomachines that generate work. Due to the nature of the working environment, turbomachines are classified as compressible flow and incompressible flow. Devices such as fans and compressors, where the incoming flow is purely air, are turbomachines with compressible flow, while devices such as hydraulic pumps, where the incoming flow is water, are turbomachines with incompressible flow. Finally, according to the direction of the flow, turbomachines are classified as axial and radial. If the inlet and outlet direction of the flow to the turbomachine are the same, it is axial, and if it is different, it is radial. [5]

Turbomachines are essential components of air-breathing jet engines. An airbreathing jet engine generates a flow of hot exhaust gases from air that is driven into the engine through multiple stages of centrifugal, axial, or ram compression before being heated and expanded through a nozzle. A typical air-breathing jet engine, the turbojet jet engine and its components are shown in figure 1.1.
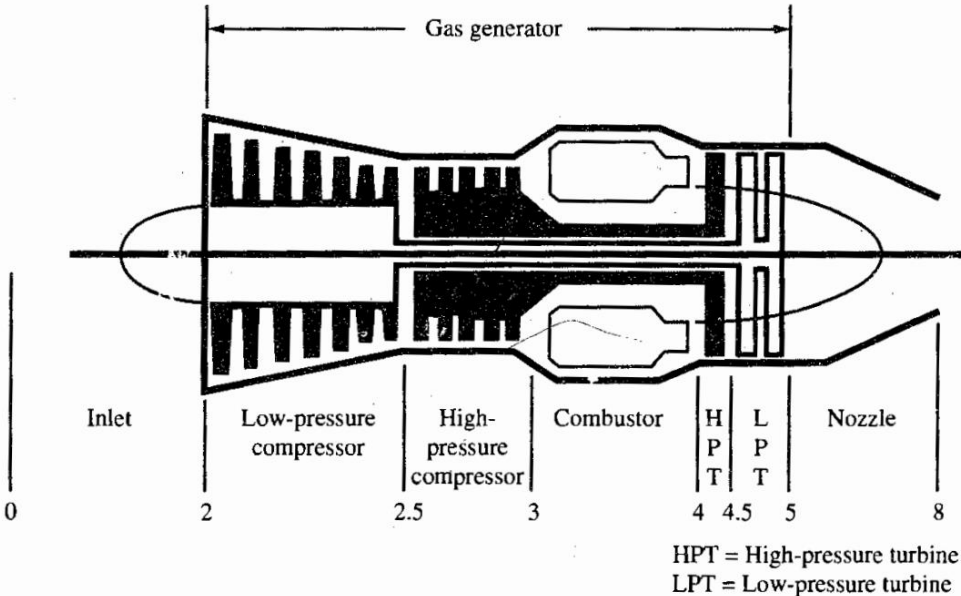
Figure 1.1: Various component of typical air-breathing jet engine. [6]

1.1 Purpose of Thesis

The aim of this thesis is to analyze only the rotor part of the transonic axial-flow NASA Stage 37 compressor by using OpenFOAM (Open Field Operation and Manupilation) software, which is an open source CFD toolbox, by examining the variation of parameters such as total pressure, total temperature and velocity along various sections on the model and compre them with experimentally obtained data.

2

1.2 Literature Review

The most important criteria for the aerospace engine performance is the thrust/weight ratio. The creation of high aspect ratio blades in the compressor, as well as adjusting the pressure ratio and firing temperature of the gas turbine for maximum work output per unit flow, result in an increase in engine thrust/weight ratio. Axial-flow compressor of a gas turbine uses between 55 and 65 percent of the power generated by the turbine section. [7]

An axial-flow compressor is one of the compressor that flow enters the compressor in an axial direction, and exits from the gas turbine also in an axial direction. Axial-flow compressors consists from combination known as stage of a rotor followed by a stator. A simple axial-flow compressor stage is shown in figure 1.2.

The main task of the axial-flow compressors is the obtain pressure rise by compressing its working fluid by first accelerating the fluid and then diffusing it. The fluid is accelerated by a row of rotating airfoils called the rotor, and then diffused in a row of stationary blades called stator. The velocity increase in the rotor is converted to a pressure rise by diffusion in the stator. In some aerospace applications, the use of numerous stages allows for overall pressure increases of up to 40:1. [7]
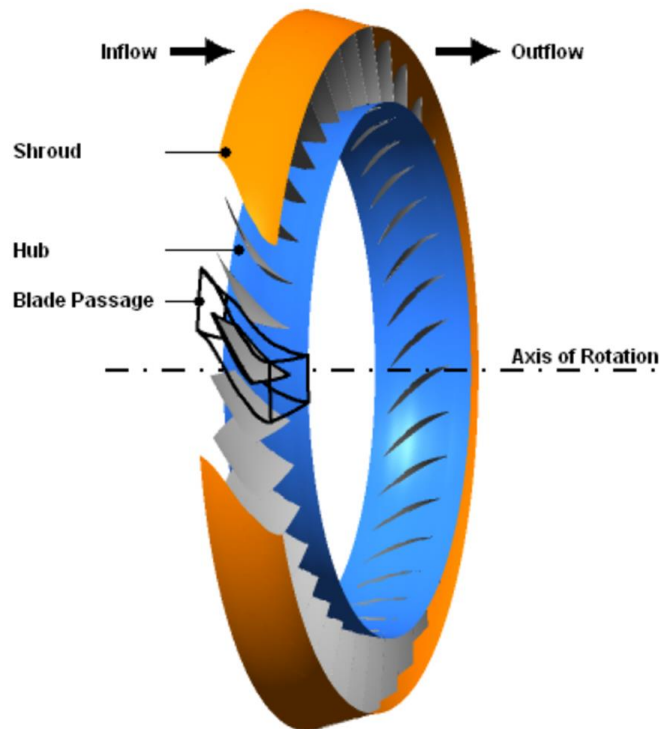
Figure 1.2: Axial-flow compressor stage. [8]

At the compressor inlet, to provide proper flow angle additional row of pitch variable blades, known as Inlet Guide Vanes (IGV), are commonly used. Thanks to the pitch variable vanes, it can be adjusted to varying flow requirements of the engine. Also, in addition to the stators, another set of vanes at the exit of the compressor, known as Exit Guide Vanes (EGV), are commonly used. Thanks to the Exit Guide Vanes (EGV) the proper fluid velocity is supplied for the combustors. The rotor rotates toward the concave side of the airfoils, which are curved on one side and convex on the other. The blade's concave side is known as the pressure side, while the convex side is known as the suction side. [7]

Table 1.1 depicts change of the parameters such as pressure, temperature, speed, enthalpy and density throughout the stage of the axial compressor. The total pressure, temperature and enthalpy increase throughout the compressor stage.

Table 1.1: Compressor-stage aerothermodynamic process. [9]

		Rotor	Stator	Stage
Static Pressure	P_{st}	↑	↑	↑
Total Pressure	P_t	↑	↓	↑
Static Temperature	T_{st}	↑	↑	↑
Total Temperature	T_t	↑	constant	↑
Relative Velocity	V_R	↓	NA	NA
Total Enthalpy	h_t	↑	constant	↑
Density	ρ	↑	↑	↑

Early low-pressure compressors had an efficiency of around 55%; the cause for this low efficiency is now attributed to stall formation on the blade. [10] The reverse pressure gradients that occur due to the rapid deceleration of the fluid throughout the compressor cause serious total pressure losses. Thus, both the rotor and the stator experience a series of diffusions. Because excessive diffusion causes separation issues, the increase in area and pressure must be moderate for compressor stages. [11] Compressor surge and choke are two phenomenon that determine the operational range of the compressor. A decrease in the mass flow rate, an increase in the rotational speed, or both cause the compressor to become unstable operation, which must be avoided, resulting in a surge situation. The compressors generally operate near the surge line. The choke point of the compressor is the point where no more flow can pass through when the flow at the blade throat reaches Mach 1.

The aerodynamic stall phenomena of the compressors arise as individual blade stall or propagating stall. Individual blade stall occurs when all of the blades surrounding the compressor annulus stall at the same time without stall propagation. Propagating stall consists of large stall zones covering several blade passages and propagates in the direction of the rotation. The number of stall zones and the rate at which they propagate differ significantly. The most common type of stall phenomenon is the propagating stall.

Any flow disturbance in front of the blade causes a stall condition on the blade as it is seen in figure 1.3. Stalled blade cannot provide sufficient pressure rise and a blockage flow zone develops. This retarded flow causes the angle of attack of the flow to the next blade to decrease and the angle of attack of the previous blade to increase. Therefore, the retarded flow or stall zone moves from the pressure side (PS) to the suction side (SS) of each blade in the opposite direction of rotor rotation. The stall zone may cover several blade passages.
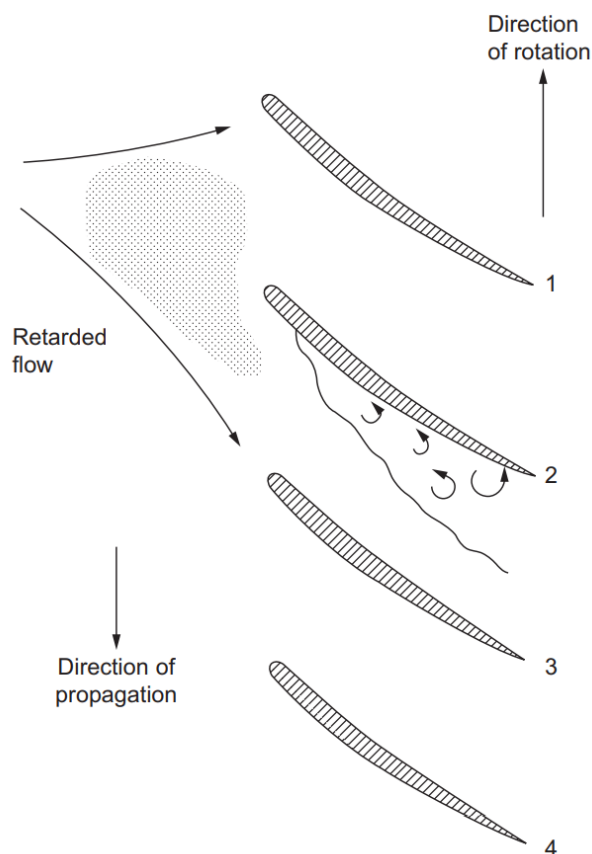

Figure 1.3: Propagating stall formation in blade cascade. [7]

Both supersonic and subsonic flow occurs in the transonic axial-flow compressors. Supersonic flow reduces the operating range of a compressor because the flow

becomes more sensitive to changes in inlet angle. However, this means a more compact, i.e. smaller compressor, providing high mass flow per unit area. Furthermore, it enables the blade speed to be provided at a higher speed, thus allowing more work input and hence higher pressure ratio.

Very thin blades are used to mitigate the effects of high Mach numbers in transonic compressors, and typical the thickness-to-chord ratio of the blades is only a few percent. Additionally, to reduce the tip mach number on the blade surface, the blades have very low camber, with only a few degrees of turning. As a result, the blade sections toward the tip of a high-speed compressor resemble sharp, thin, and almost flat plates. [10]
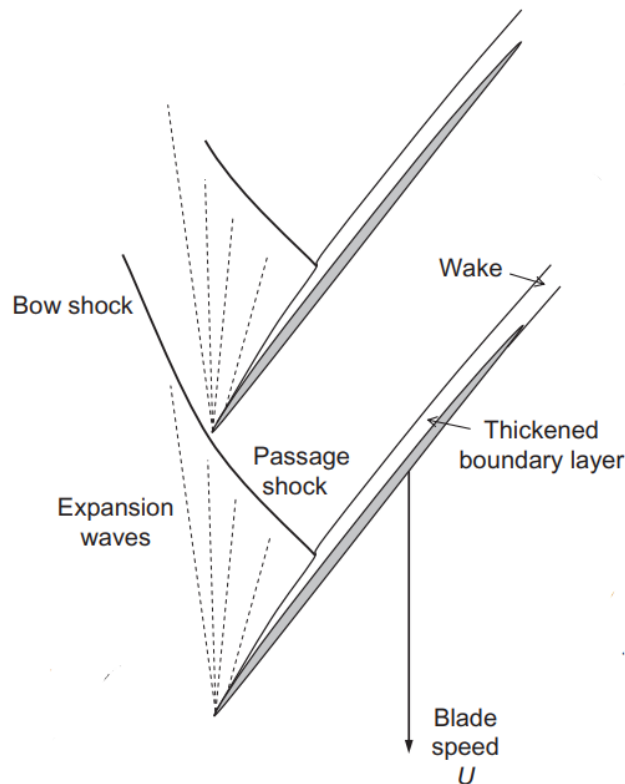
Figure 1.4: Flow through a supersonic compressor rotor. [10]

The position of the shock wave changes as the operating point of the compressor changes. When the flow is completely choked, the shock moves backwards within the blade passage to be completely engulfed. At lower mass flow rates, the shock wave is ejected in front of the blade passage when the compressor is closer to stall. The operating point corresponding to the highest efficiency usually occurs when the shock wave is near the leading edge of the blade as it is shown in figure 1.4. [10]

1.3 Outline

In this part of the thesis, basic information is given in order to understand the study to be done. In this context, basic information about computational fluid dynamics (CFD), the purpose of using axial compressors and various situations that may occur during flow are briefly mentioned. In the second part, the Navier-Stokes equations, which are the mathematical equations in the background of computational fluid dynamics (CFD), is discussed. In the third part, the configuration of the study that are the construction of the solid model, the determination of the boundary conditions, the creation of the mesh structures, the selection of the solver and the discussion of the results of the analysis are mentioned. In the last part, conclusion and future work are mentioned.

2 GOVERNING EQUATIONS

The mathematical basis of computational fluid dynamics (CFD) used in the analysis
and solution of flow problems is based on conservation laws of physics known as
Navier-Stokes equations. The Navier-Stokes equations are based on the principles of
conservation of mass, momentum and energy and these equations presented in the
following section for three-dimensional flows in differential form. Also, since most
flows are turbulent with fluctuations of pressure, temperature and velocity over a wide
range of frequencies, these quantities decomposes into a mean part and a fluctuating
part and the averaging the equations leads to the Reynolds-averaged Navier-Stokes
(RANS) equations which govern the mean flow. As a RANS equation, k-epsilon
turbulence model has been presented in this study.

2.1 The Continuity Equation

Matter cannot be generated or destroyed, according to one conservation law applicable
to fluid flow. The continuity equation can be expressed as

$$\frac{\partial \rho}{\partial t} + \nabla . (\rho \mathbf{V}) = 0 \qquad \textbf{(2.1)}$$

where ρ is density and $\mathbf{V}$ is the velocity.

2.2 The Momentum Equation

Momentum is defined as product of mass and velocity of an element. Newton's second
law of motion states that the rate of change of momentum of an element over time is
directly proportional to the force applied, and occurs in the same direction as the
applied force. The momentum equations in the x, y, and z directions, respectively, can
be expressed as

$$\frac{\partial(\rho u)}{\partial t} + \nabla.(\rho u \mathbf{V}) = -\frac{\partial p}{\partial x} + \frac{\partial \tau_{xx}}{\partial x} + \frac{\partial \tau_{yx}}{\partial y} + \frac{\partial \tau_{zx}}{\partial z} + \rho f_x \qquad \textbf{(2.2a)}$$

$$\frac{\partial(\rho v)}{\partial t} + \nabla.(\rho v \mathbf{V}) = -\frac{\partial p}{\partial y} + \frac{\partial \tau_{xy}}{\partial x} + \frac{\partial \tau_{yy}}{\partial y} + \frac{\partial \tau_{zy}}{\partial z} + \rho f_y \qquad \textbf{(2.2b)}$$

$$\frac{\partial(\rho w)}{\partial t} + \nabla.(\rho w \mathbf{V}) = -\frac{\partial p}{\partial z} + \frac{\partial \tau_{xz}}{\partial x} + \frac{\partial \tau_{yz}}{\partial y} + \frac{\partial \tau_{zz}}{\partial z} + \rho f_z \qquad \textbf{(2.2c)}$$

where ρ is density, p is the pressure, f is the body force acting on fluid element and τ is the shear stress.

2.3 The Energy Equation

The law of conservation of energy, the first law of thermodynamics, states that the total energy of an isolated system is constant; energy cannot be created or destroyed. It can, however, be transferred from one location to another and converted to and from other forms of energy. The first law of thermodynamics:

$$\begin{aligned}
&Time\ rate\ of\ change\ of\ energy \\
&= Net\ rate\ of\ heat\ added\ \left(\sum \dot{Q}\right) \\
&+ Net\ rate\ of\ work\ done\ \left(\sum \dot{W}\right)
\end{aligned} \qquad \textbf{(2.3)}$$

The energy equation can be expressed as

$$\frac{\partial}{\partial t}\left[\rho\left(e+\frac{V^2}{2}\right)\right] + \nabla.\left[\rho\left(e+\frac{V^2}{2}\mathbf{V}\right)\right]$$

$$= \rho\dot{q} + \frac{\partial}{\partial x}\left(k\frac{\partial T}{\partial x}\right) + \frac{\partial}{\partial y}\left(k\frac{\partial T}{\partial y}\right) + \frac{\partial}{\partial z}\left(k\frac{\partial T}{\partial z}\right)$$

$$-\frac{\partial(up)}{\partial x} - \frac{\partial(vp)}{\partial y} - \frac{\partial(wp)}{\partial z}$$

$$+\frac{\partial(u\tau_{xx})}{\partial x} + \frac{\partial(u\tau_{yx})}{\partial y} + \frac{\partial(u\tau_{zx})}{\partial z} \tag{2.4}$$

$$+\frac{\partial(v\tau_{xy})}{\partial x} + \frac{\partial(v\tau_{yy})}{\partial y} + \frac{\partial(v\tau_{zy})}{\partial z}$$

$$+\frac{\partial(w\tau_{xz})}{\partial x} + \frac{\partial(w\tau_{yz})}{\partial y} + \frac{\partial(w\tau_{zz})}{\partial z} + \rho\mathbf{fV}$$

where ρ is density, e is the internal energy, p is the pressure, V is the velocity, T is the temperature, f is the body force acting on fluid element and τ is the shear stress. The term $e + V^2/2$ is the total energy.

The preceding Eq. (2.1), Eq. (2.2) and Eq. (2.4) are the Navier-Stokes equations in the conservation form for the viscous flow which includes the dissipative, transport phenomena of viscosity and thermal conduction.

Continuity equation, momentum equation and conservation of energy equations are presented from computational fluid dynamics written by Wendt. [12]

2.4 The Standart k-ε Turbulence Model

Since ε appears directly in the k equation in the $k - \varepsilon$ turbulence model, this model is preferred because it offers economic computational costs for many flow problems in CFD.

According to the Launder & Spalding [13] the turbulent kinetic energy dissipation rate (ε) equation at high number may be expressed as

$$\frac{D\varepsilon}{Dt} = \frac{1}{\rho}\frac{\partial}{\partial x_k}\left[\frac{\mu_t}{\sigma_\varepsilon}\frac{\partial\varepsilon}{\partial x_k}\right] + \frac{C_1\mu_t}{\rho}\frac{\varepsilon}{k}\left(\frac{\partial U_i}{\partial x_k}+\frac{\partial U_k}{\partial x_i}\right)\frac{\partial U_i}{\partial x_k} - C_2\frac{\varepsilon^2}{k} \tag{2.5}$$

According to the Launder & Spalding [13] the turbulent kinetic energy (k) equation at high number may be expressed as

$$\frac{Dk}{Dt} = \frac{1}{\rho}\frac{\partial}{\partial x_k}\left[\frac{\mu_t}{\sigma_k}\frac{\partial k}{\partial x_k}\right] + \frac{\mu_t}{\rho}\left(\frac{\partial U_i}{\partial x_k} + \frac{\partial U_k}{\partial x_i}\right)\frac{\partial U_i}{\partial x_k} - \varepsilon \qquad \textbf{(2.6)}$$

where ρ is density and μ_t is the turbulent viscosity. The turbulent viscosity equation as follows

$$\mu_t = C_\mu \frac{\rho k^2}{\varepsilon} \qquad \textbf{(2.7)}$$

The constant values for the Eq. (2.5), Eq. (2.6) and Eq. (2.7) are $C_\mu = 0.09$, $C_1 = 1.44$, $C_2 = 1.92$, $\sigma_k = 1.0$ and $\sigma_\varepsilon = 1.3$.

3 CONFIGURATION OF THE STUDY

To perform the analysis, the solid model of NASA Rotor 37 was first created. Then, the mesh structure of the solid model was created. Finally, the initial and boundary conditions were determined and the analysis was performed using the OpenFOAM v9 version. The obtained results are presented and compared with the experimental data obtained by Suder, K. L. in Ref. [14].

3.1 OpenFOAM

OpenFOAM is an open source software written in C++ for computational fluid dynamics (CFD). OpenFOAM offers solutions for a wide range of engineering problems.

Since OpenFOAM is an open source software, there are many different versions. For this study, OpenFOAM v9 version offered by The OpenFOAM Foundation was used. All analysis was performed on Ubuntu 21.04 (Hirsute Hippo) operating system.

3.2 NASA Rotor 37 Geometry Generation

In this study, the 3D solid model of NASA Rotor 37, shown in figure 3.1, was created twice. To create 3D model Siemens NX 12 and ANSYS TurboGrid 19.2 softwares were used. Although both 3D solid model created are identical, two different software were used because they provide various conveniences in the computational domain creation stage.
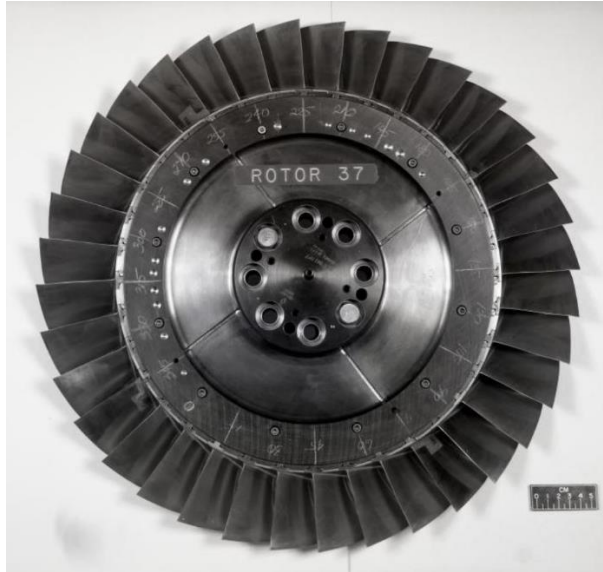
**Figure 3.1:** Wheel assembly of NASA Rotor 37. [15]
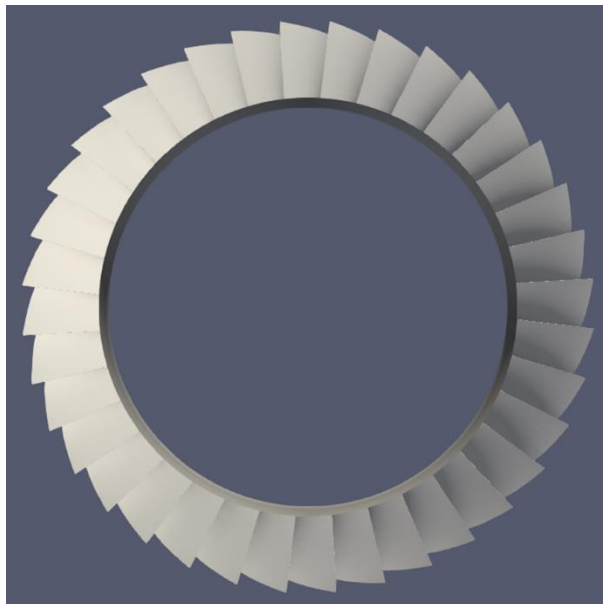
Figure 3.2: Displaying hub and blade parts of the created 3D model of NASA Rotor 37 on Paraview.

The manufacturing coordinates of Rotor 37 have been presented in the report that is performed by Reid, L., & Moore, R. D. in Ref. [16]. The design specifications of NASA Rotor 37 have been presented in Table 3.. Displaying hub and blade parts of the created CAD of 3D model of NASA Rotor 37 on Paraview is shown in Figure 3.2.

To perform the analysis of the 36-blade Rotor 37, a 3D model of the passage, consisting of only 1 blade, was created. The single-blade passage is going to save time and computational power for analysis.
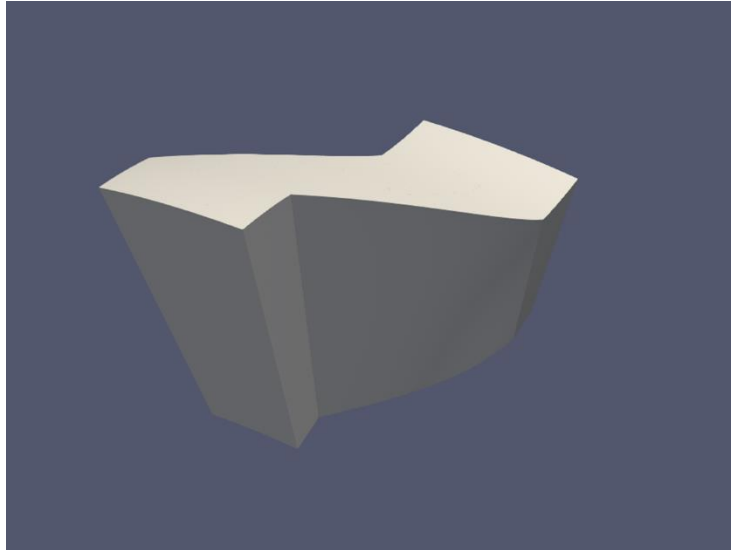
(a)
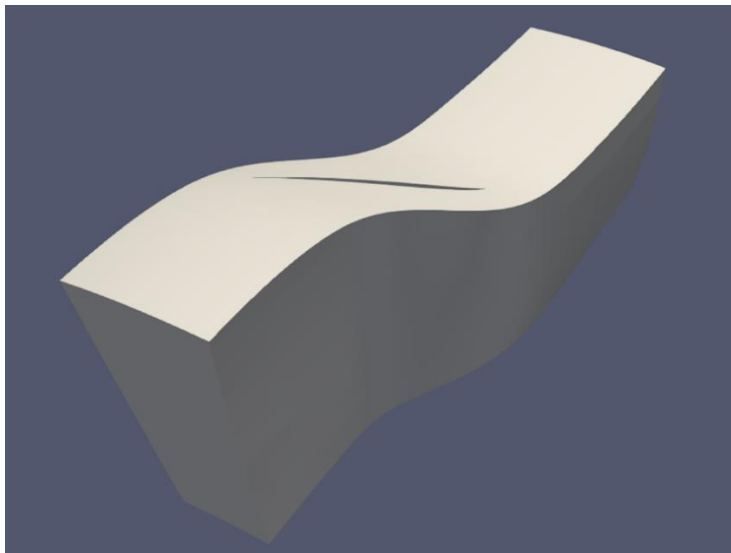
(b)

Figure 3.3: (a) Passage of a 3D model of NASA Rotor 37 created with Siemens NX 12 (b) Passage of a 3D model of NASA Rotor 37 created with ANSYS Turbogrid 19.2.

Figure 3.3 shows a passage of a 3D model of NASA Rotor 37 created with both Siemens NX 12 and ANSYS Turbogrid 19.2. Since the solution diverges, the tip clearance neglected at the model created with ANSYS TurboGrid.

Design specifications of NASA Rotor 37 have been tabulated in Table 3.1.

Table 3.1: Design specifications of NASA Rotor 37. [17]

Parameter	Value
Number of rotor blades	36
Rotational speed (rpm)	17188.7
Rotor inlet hub-to-tip diameter ratio	0.7
Rotor tip solidity	1.29
Rotor blade aspect ratio	1.19
Tip clearance (design) (mm)	0.356 (at 47 % span)
Tip speed (m/s)	454.136
Blade airfoil sections	Multiple-Circular-Arc
Design mass flow rate (kg/s)	20.19
Mass flow choking (kg/s)	20.93
Reference pressure (Pa)	101325
Total pressure ratio	2.106
Rotor tip relative inlet Mach number	1.48
Rotor hub relative inlet Mach number	1.13
Reference temperature (K)	288.15
Rotor polytrophic efficiency	0.889

3.3 Mesh Generation

Meshing is the process by which an object is divided into thousands or more small shapes to accurately describe the physical shape of the object. The more detailed a mesh is, the more accurate the analysis result will be, but it should be noted that resolving very detailed mesh requires a lot of computational power and time. Therefore, creating the most suitable mesh structure is the basis of a good analysis.

In this study created two passages have been meshed. The 3D model of the passage that is created by Siemens NX 12 has been meshed with snappyHexMesh utility of OpenFOAM. The mesh structure obtained by snappyHexMesh utility is shown in figures 3.4. The mesh structure in the leading edge (LE) and trailing edge (TE) parts of the blade section 50% span from hub shown in figure 3.5.
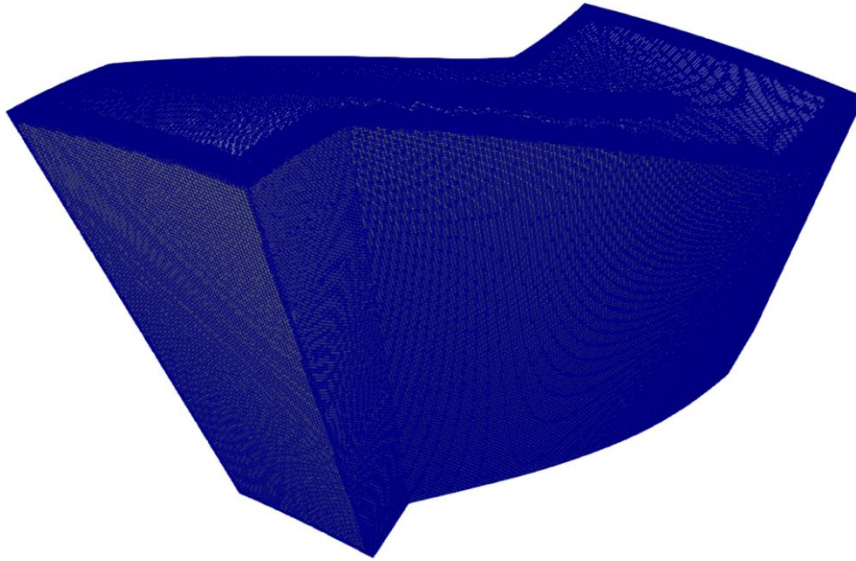
**Figure 3.4:** snappyHexMesh structure of NASA Rotor 37.

To check meshing quality of R37 snappyHexMesh, the checkMesh utility of the OpenFOAM has been used and the results have been presented in Table 3.2.

Table 3.2: A checkMesh utility results of R37 with snappyHexMesh.

Parameter	Value
Number of cell	1192428
Max skewness	3.55
Max non-orthogonality	63.72
Max aspect ratio	9.76
Min volume	2.88e-14
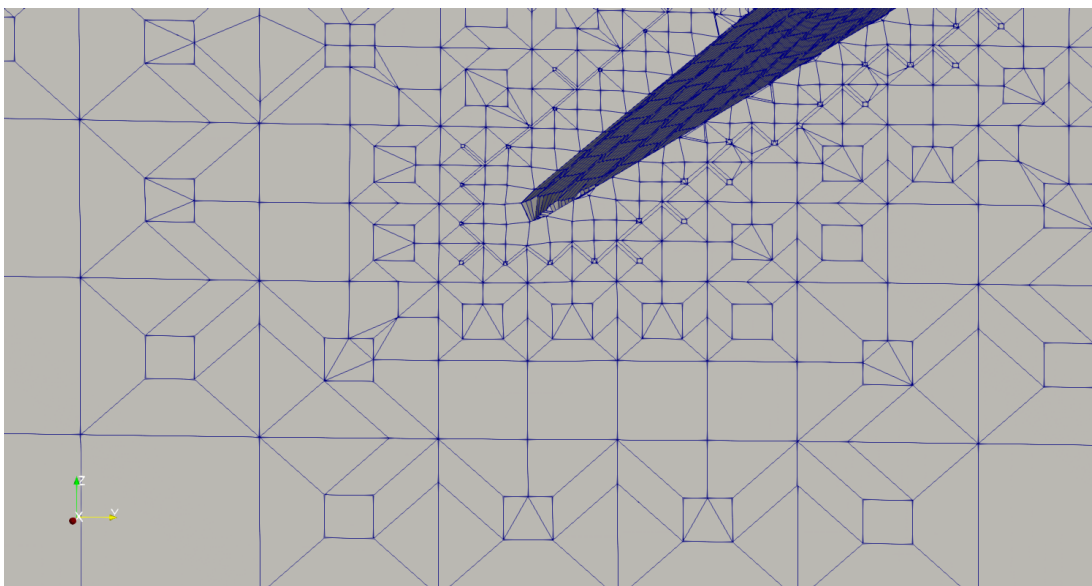
(a)
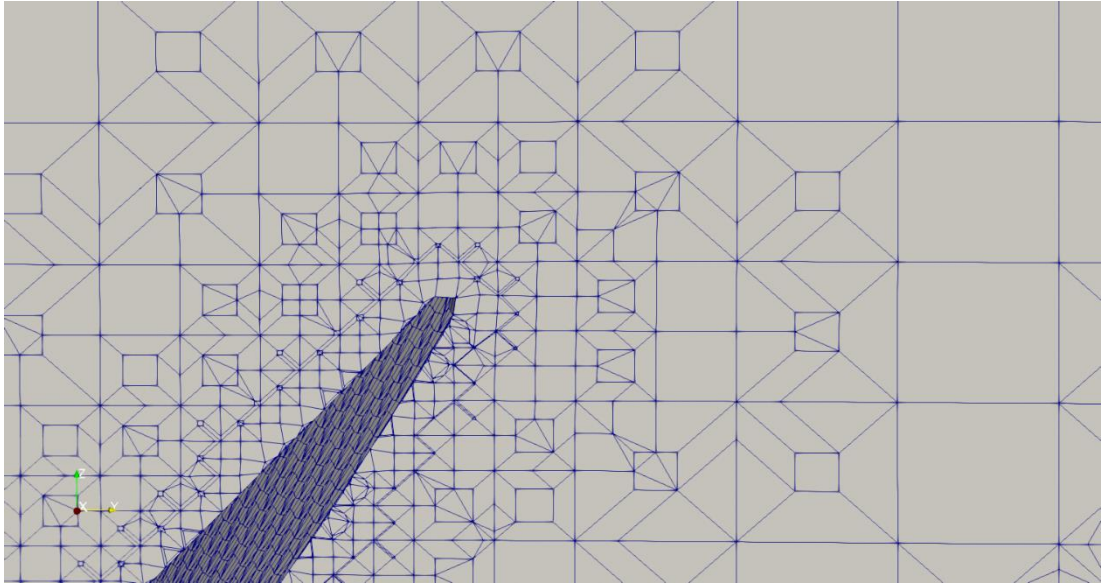
(b)

Figure 3.5: (a) Leading edge part of the blade section 50% span from hub, (b) Trailing edge part of the blade section 50% span from hub.

Due to the bad cell condition on the blade leading edge (LE), trailing edge (TE) and the shroud tip sections solution has diverged. Therefore, the solution cannot proceeded by using snappyHexMesh. Therefore, To obtain results of the study, the 3D model created by using ANSYS TurboGrid exported to the ANSYS Fluent in order to get proper extension for the FluentMeshToFoam utility of OpenFOAM. Then, using the FluentMeshToFoam utility hexahedral mesh structure of the R37 has obtained as shown in Figure 3.6.
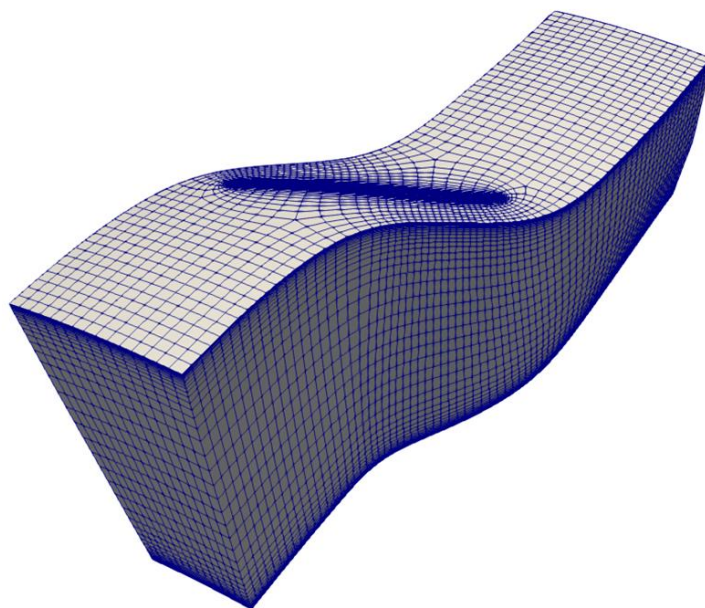

Figure 3.6: The hexahedral mesh structure of NASA Rotor 37.

To check meshing quality of R37 hexahedral mesh, the checkMesh utility of the OpenFOAM has been used and the results have been presented in Table 3.3.
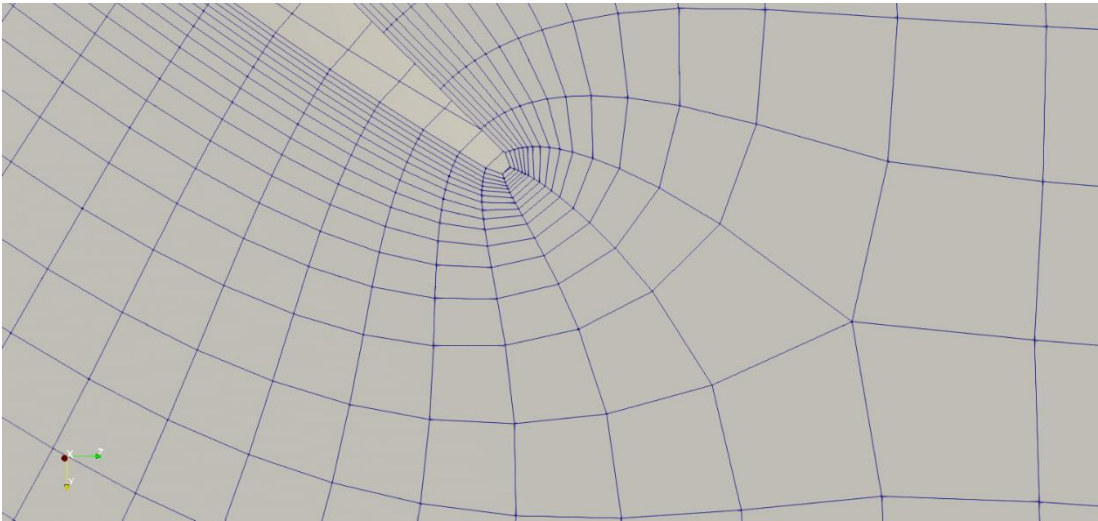
Table 3.3: A checkMesh utility results of R37 with hexahedral mesh.

Parameter	Value
Number of cell	85011
Max skewness	2.34
Max non-orthogonality	36.32
Max aspect ratio	35.56
Min volume	5.2e-08

In figure 3.7, the leading edge (LE) and trailing edge (TE) parts of the blade section that is the mid section of the domain shown in figure 3.6 has presented.
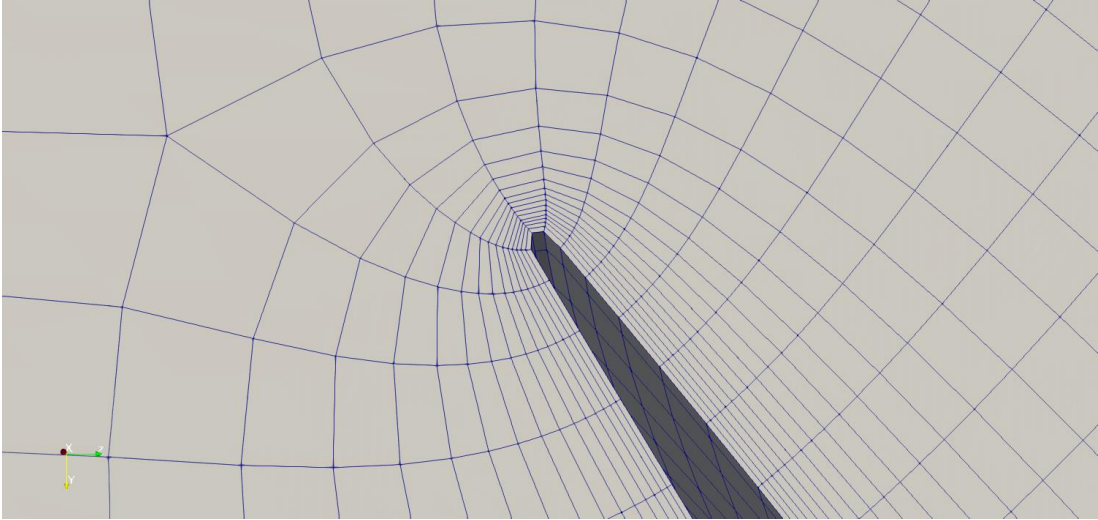
(a)

(b)

Figure 3.7: (a) Leading edge part of the blade section 51% span from hub, (b) Trailing edge part of the blade section 51% span from hub.

Since the solution is going to diverges, the tip clearance has been neglected in the R37 hexahedral mesh.

To summarize, to obtain results the hexahedral mesh structure of R37 shown in Figure 3.6 has used as the computational domain.

3.4 Boundary Conditions

Correct CFD analysis is achieved by successfully solving the derived partial differential equations. Therefore, for each physical quantity to be solved, the boundary condition must be defined at each boundary of the defined numerical domain.
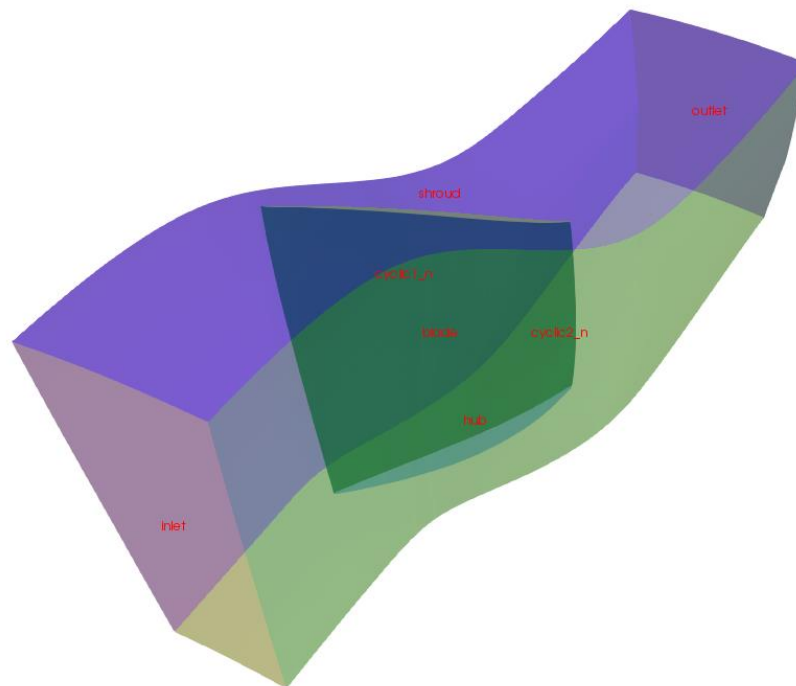
Figure 3.8: Patches of R37 computational domain.

In Figure 3.8, the patch topology of the computational domain created for this study is shown, and in table 3.4 the types of patch topology are listed.

Table 3.4: A Patch topology for NASA Rotor 37.

Patch name	Patch type
inlet	patch
outlet	patch
hub	wall
shroud	wall
blade	wall
cyclic1_n	cyclicAMI
cyclic2_n	cyclicAMI

Table 3.5 lists the applied boundary conditions for pressure, velocity and temperature at the defined boundaries. totalPressure boundary condition was imposed on the inlet patch and the corresponding total pressure value is set to 101325 Pa. fixedValue boundary condition was imposed on the outlet patch and the corresponding static pressure value is set to 120500 Pa. [18]

pressureDirectedInletVelocity boundary condition was imposed on the inlet patch. The velocity value was calculated from the pressure. Therefore, this condition applies where pressure value is specified. totalTemperature boundary condition was imposed on the inlet patch and the corresponding total temperature value is set to 288.15 K. [18] inletOutlet boundary condition was imposed on the outlet patch for velocity and zeroGradient for temperature. fixedValue boundary conditions for velocity means no-slip boundary condition.

Since the NASA Rotor 37 is a rotating axial compressor, the rotation effect has taken into account by using multi reference frame (MRF) approach. To set the rotation effect, cellZone consisting of a set of rotating cells was generated and imposed to 17188.7 rpm which is equal to the 1800 rad/s. The generated rotating cellZone covers the complete grid of finite volumes. In addition, the inlet, outlet, hub and shroud patches was set as nonrotating patches.

Table 3.5: Boundary conditions of the pressure, velocity, and temperature.

| Patch name	Pressure (0/p)	Velocity (0/U)	Temperature (0/T)
inlet	totalPressure	pressureDirectedInletVelocity	totalTemperature
outlet	fixedValue	inletOutlet	zeroGradient
hub	zeroGradient	fixedValue	zeroGradient
shroud	zeroGradient	fixedValue	zeroGradient
blade	zeroGradient	fixedValue	zeroGradient
cyclic1_n	cyclicAMI	cyclicAMI	cyclicAMI
cyclic2_n	cyclicAMI	cyclicAMI	cyclicAMI

3.5 Numerical Details

The rhoSimpleFoam solver which is a steady-state solver for compressible, turbulent flow, using the SIMPLE (Semi-Implicit Method for Pressure Linked Equations) algorithm of OF was used for this study. [19] rhoSimpleFoam is a pressure based compressible solver. The k-epsilon model was chosen as the turbulence model.

The computational domain that is obtained by using snappyHexMesh utility was not performed for the solution. This may be due to the divergence of results in some regions within the domain due to poor mesh quality. Therefore, the results are obtained for the computational domain that are obtained with fluentMeshToFoam.

3.6 Results

In order to display the 3D analysis results of the R37 and compare them with the experimental results, first, it is necessary to know from which region of the computational domain the data in the experimental study were taken. The coordinates at which the measurements of the experimental results obtained by Suder, K. L. in Ref. [14] are shown in AGARD report 335.
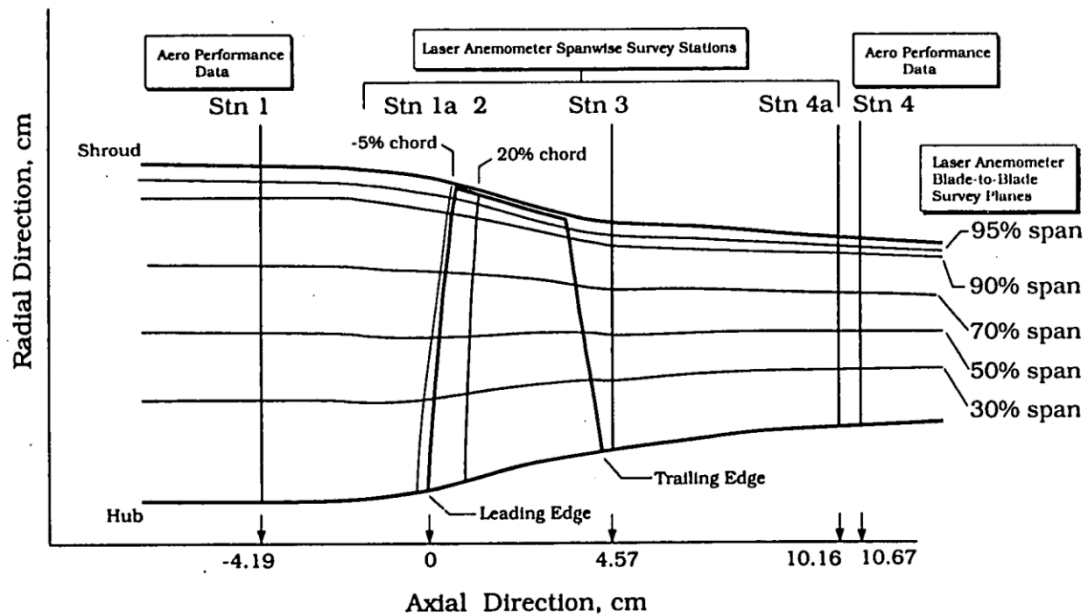
Figure 3.9: Measurement stations. [20]

Table 3.6 lists the experimental and cfd results. While the total pressure ratio obtained according to the CFD analysis is less than the experimental study, the total temperature ratio is higher than the experimental study. The mass flow rate is almost the same for both studies.

Table 3.6: A Patch topology for NASA Rotor 37.

Parameter	CFD	Design Value
Rotor Total Pressure Ratio	1.76	2.106
Rotor Total Temperature Ratio	1.38	1.270
Mass Flow, kg/s	20.68	20.188

The results obtained in figures 3.10 and 3.11 were obtained for station 4 shown in figure 3.9. Stations 1 and 4 also correspond to the inlet and outlet patches in the computational domain respectively.
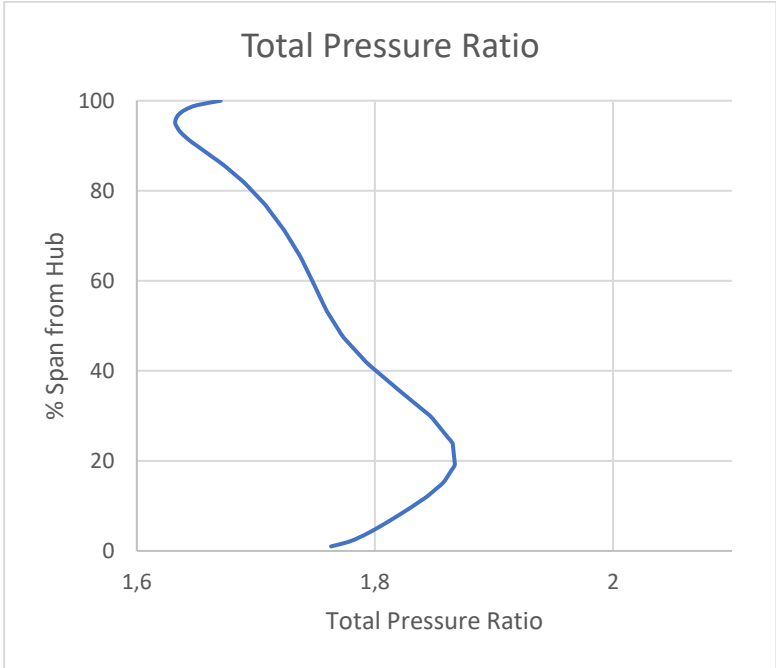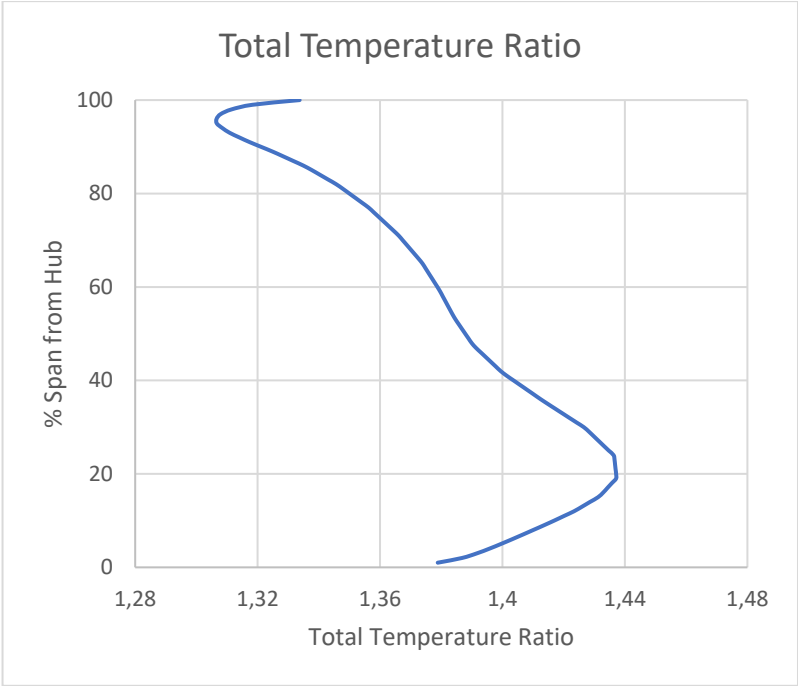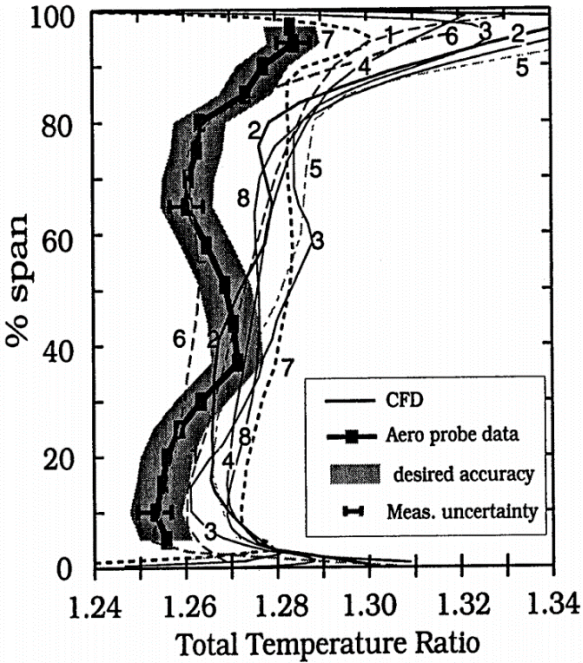

(a)
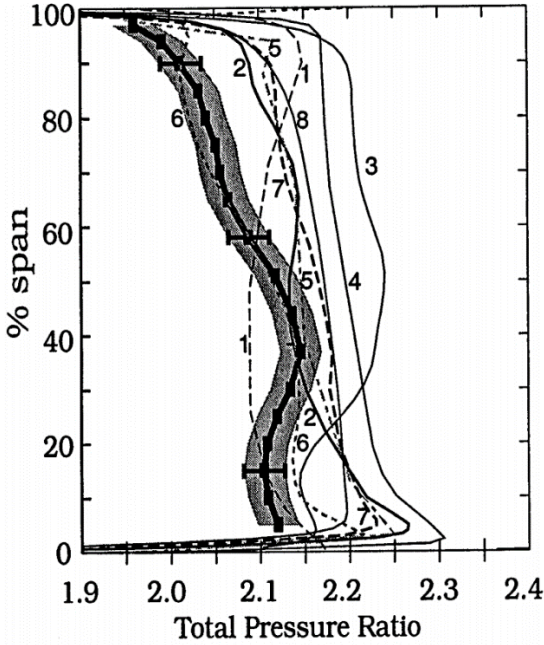
(b)

Figure 3.10: Total pressure ratio result of (a) CFD and (b) experimental studies. [14]

(a)

(b)

Figure 3.11: Total temperature ratio result of (a) CFD and (b) experimental studies.
[14]

As shown in Figure 3.10, the CFD analysis result and the experimental result are different from each other, but the trends in the result of the CFD analysis are in agreement with the experimental result. The upward trend in the overall pressure ratio

from the hub to the shroud occurs closer to the hub in the experimental study. The decreasing trend of the increase in the total pressure ratio occurs in 20% span from hub in the CFD analysis and 5% span from hub in the experimental study. The tendency of the total pressure ratio in the CFD analysis to increase again near 10% span from shroud may be due to the neglect of the tip clearance in the computational domain.

The total temperature ratio obtained as a result of the CFD analysis shown in Figure 3.11 appears to be quite different from the experimental results. This difference could be due to the poor mesh quality or neglecting tip clearance effect for the computational domain.

As can be seen in Table 3.6, figure 3.10 and figure 3.11, in the results obtained as a result of the CFD analysis, the fact that the total pressure ratio is greater than 1 indicates that the compressor performs its main task, which is compression. However, the fact that the total temperature ratio obtained as a result of the CFD analysis is higher than the experimental result, but the total pressure ratio is low, shows that the compressor does a lot of work but does not provide sufficient compression ratio in return for this work. In other words, according to the results of the CFD analysis, it is concluded that the compressor is an inefficient compressor.

Figures 3.12, 3.13 and 3.14 show the relative Mach number, total pressure ratio, and total temperature ratio at 20%, 51%, and 80% span from the hub, respectively.

In Figure 3.12, it is seen that the bow shock waves formed in the leading edge of the blade hit the suction side of the other blade. The relative Mach number reaches its highest value mid-section of the blade at the suction side, while it reaches its minimum value at the trailing edge at suction side. As the shroud is approached, it is seen that the shock waves formed due to the increase in relative velocity become stronger and moves through to trailing edge. In addition, the relative Mach number in the entrance passage is greater than the exit passage, indicating that the air slows down during compression.
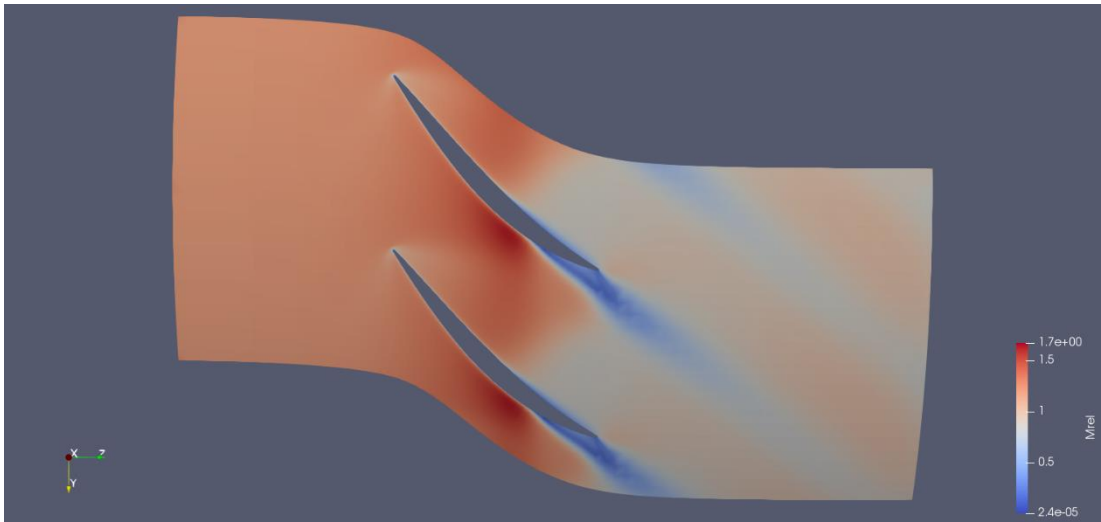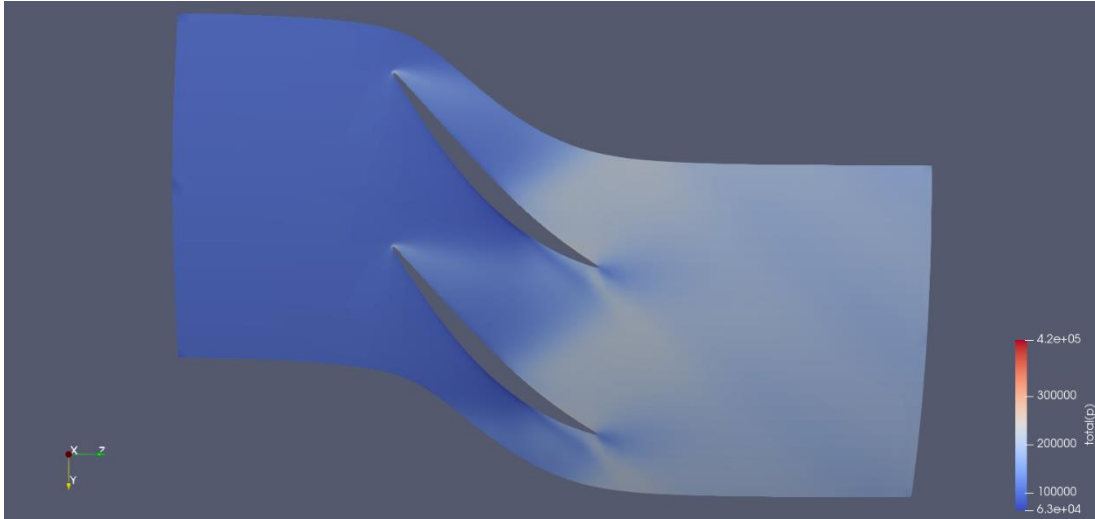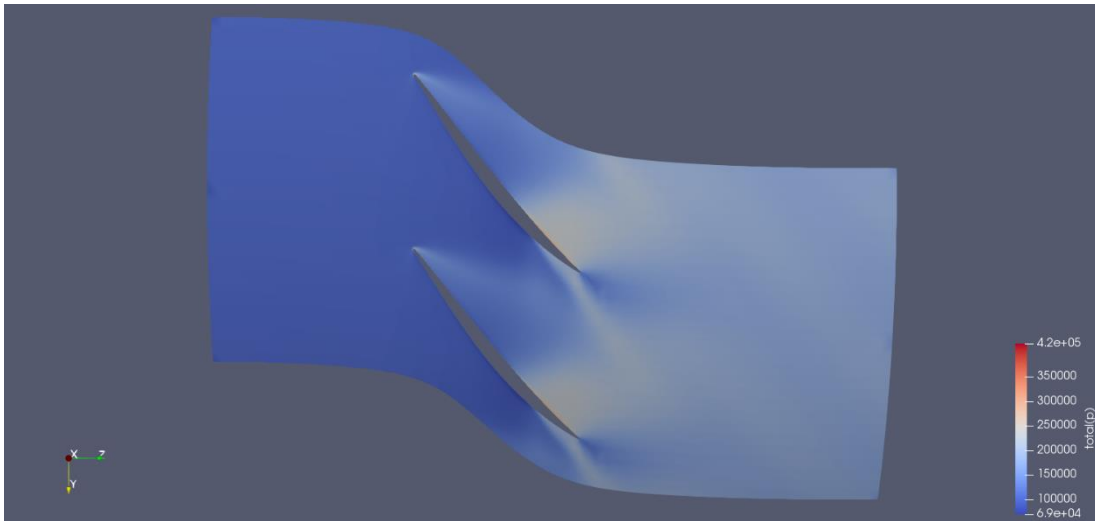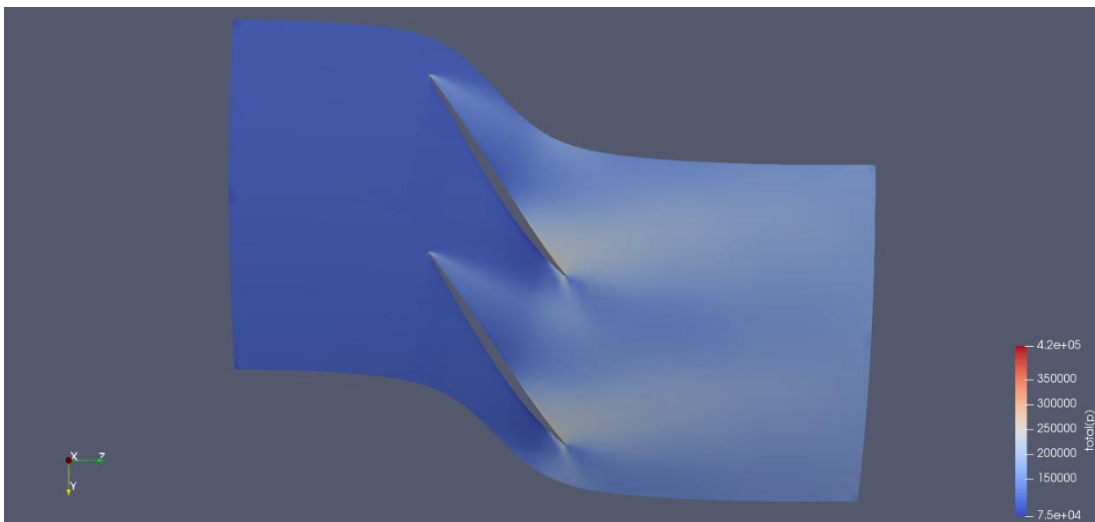
(a)
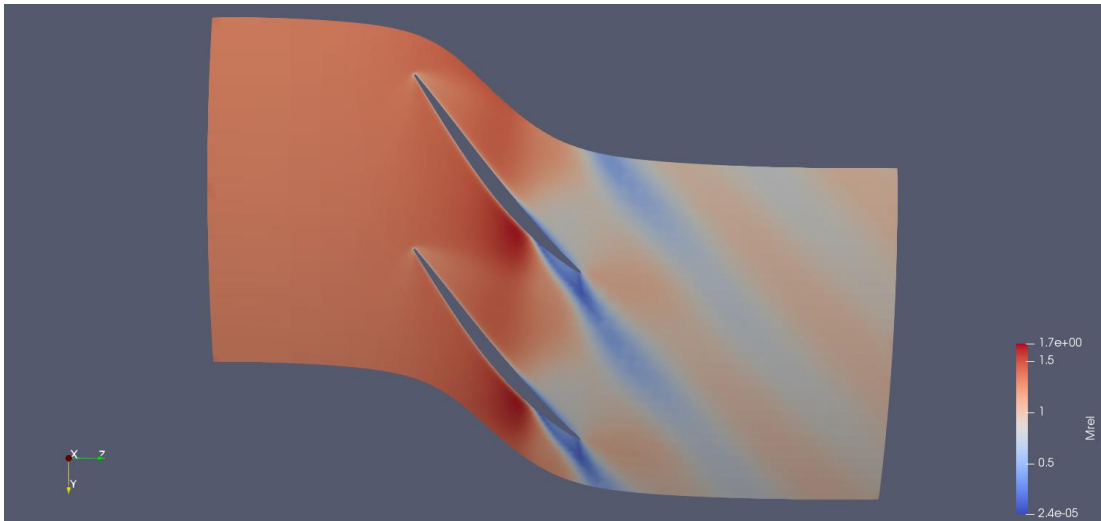
(b)
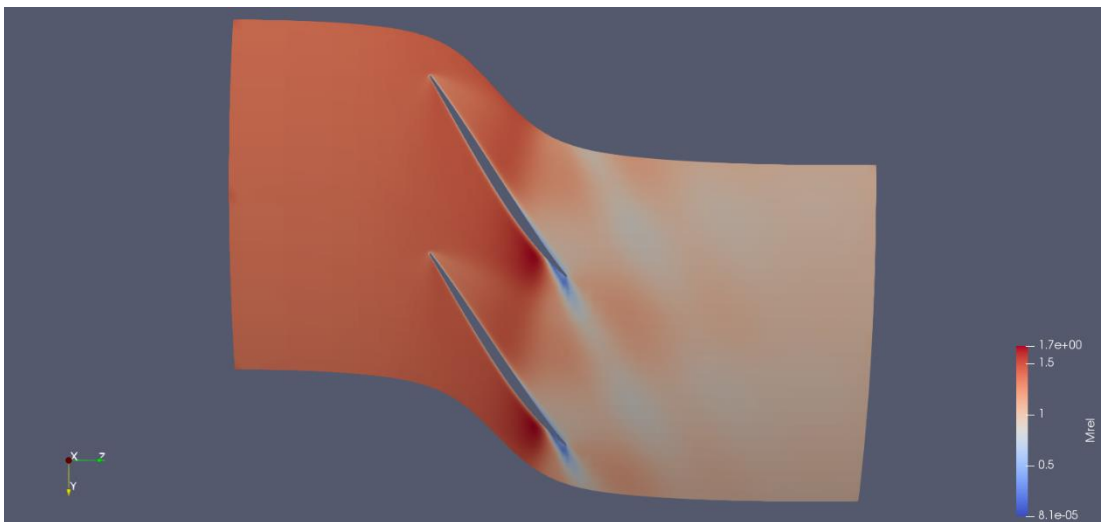
(c)

Figure 3.12: Relative mach number slice (a) 20% (b) 51% (c) 80% span from hub.
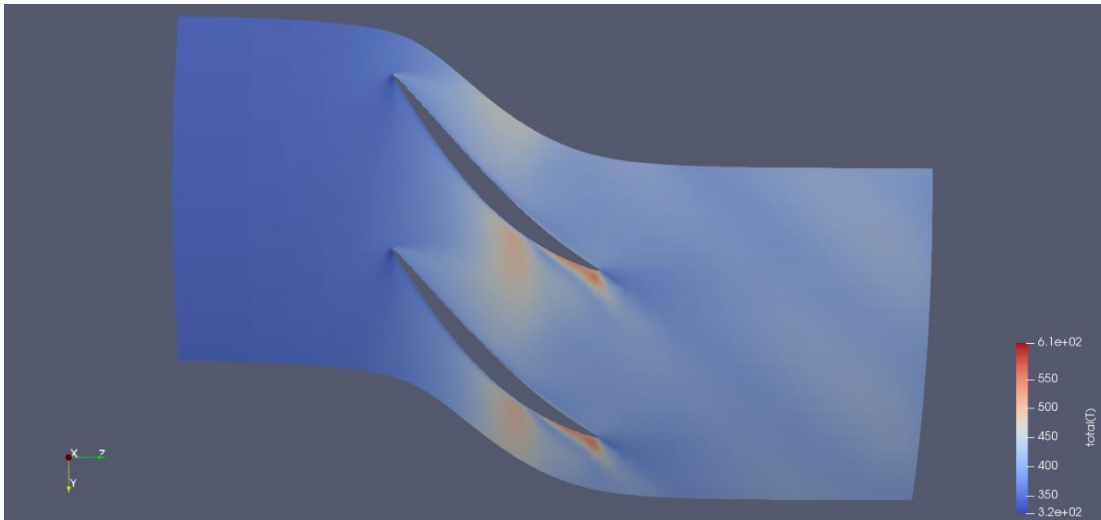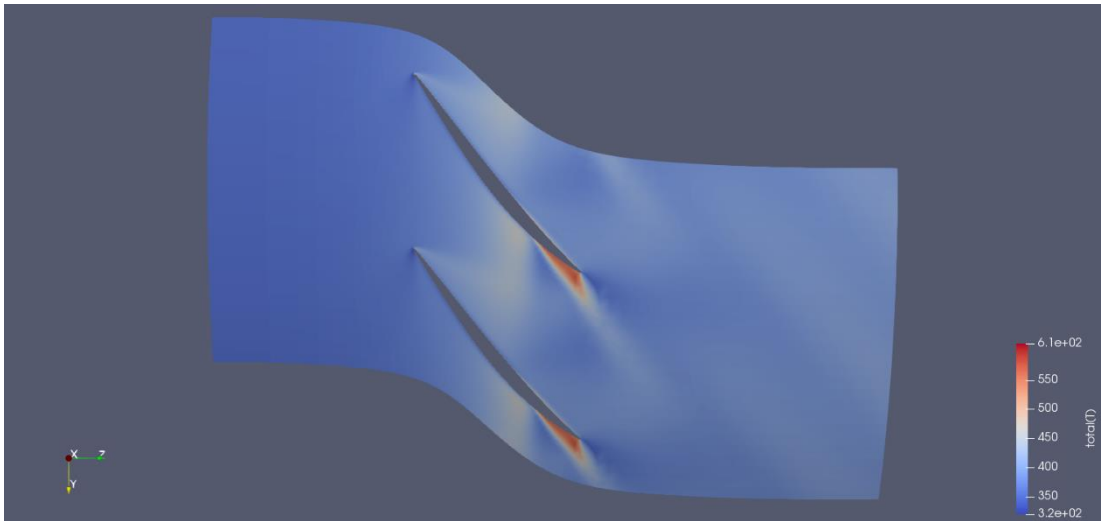
(a)

(b)

(c)

Figure 3.13: Total pressure slice (a) 20% (b) 51% (c) 80% span from hub.

(a)

(b)
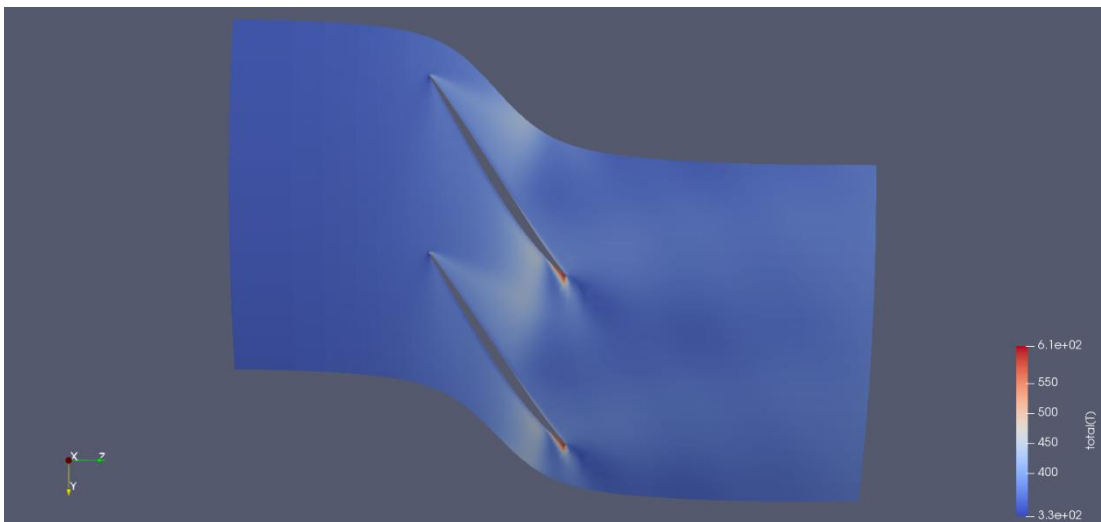
(c)

Figure 3.14: Total temperature slice (a) 20% (b) 51% (c) 80% span from hub.

In Figure 3.13, it is seen that the total pressure ratio decreases as the shroud is approached, but as can be seen in the slices taken from 20%, 51% and 80% span from hub, the total pressure ratio is greater than 1, that is, the compressor fulfills its main task. In figure 3.14, it's clear that the total temperature ratio decreases through to the shroud and it's always greater than 1.

4 CONCLUSION AND FUTURE WORK

In this study, numerical analysis of NASA Rotor 37, an axial compressor, was performed. Since the R37 is a transonic compressor, it is very important to establish the computational domain. Computational domain was created with ANSYS TurboGrid and converted to convenient format for OpenFOAM. In order to reduce the computational cost and time in the analysis of the R37, which consists of 36 blades, mesh of single passage was created.

OpenFOAM v9 version was used as analysis program in the study. Total pressure and temperature ratios were compared with experimental data. Although the CFD analysis did not fit the experimental data with the desired precision, they indicated a similar tendency. In the study, rhoSimpleFoam was used as solver, k-epsilon model was used as turbulence model and MRF approach was used.

The results obtained in the study are different from the experimental results. This could be due to the poor mesh quality, especially the mesh of the leading and trailing edges of the blade, which is not of sufficient quality for the formation of shock waves. Also, ignoring the tip clearance effect may be the reason for these differences.

The mesh quality of the computational domain can be increased to obtain more accurate analyzes in future studies. Different levels of refinements can be used, especially for the leading and trailing edge of the blade. By increasing the number of cells in the computational domain, the tip clearance effect can be included in the analysis.

5 PREFERENCES

[1] **Hami, K.** (2021). Turbulence Modeling a Review for Different Used Methods. *International Journal of Heat & Technology, 39*(1), 227–234. https://0-doi-org.divit.library.itu.edu.tr/10.18280/ijht.390125

[2] **Pinto, R. N., Afzal, A., D, S. L. V., Ansari, Z., & Mohammed Samee, A. D.** (2017). Computational Fluid Dynamics in Turbomachinery: A Review of State of the Art. *Archives of Computational Methods in Engineering: State of the Art Reviews, 24*(3), 467. https://0-doi-org.divit.library.itu.edu.tr/10.1007/s11831-016-9175-2

[3] **Aviation industry update.** (1994), *Aircraft Engineering and Aerospace Technology, 66*(1), 7-9. https://doi.org/10.1108/eb037460

[4] **Rajadurai, J. S.** (2003). *Thermodynamics and Thermal Engineering*. New Age International (P) Limited.

[5] **Baskharone, E. A.** (2006). *Principles of Turbomachinery in Air-Breathing Engines (Cambridge Aerospace Series, Series Number 18)* (1st ed.). Cambridge University Press.

[6] **Mattingly, J. D.** (2005). *Elements Of Gas Turbine Propulsion*. McGraw-Hill Education.

[7] **Boyce Fellow American Society of Mechanical Engineers (ASME USA) and Fellow The Institute of Diesel and Gas Turbine Engineers (IDGTE U.K.), Meherwan P.** (2011). *Gas Turbine Engineering Handbook* (4th ed.). Butterworth-Heinemann.

[8] **ANSYS TurboGrid Tutorials** (2015). *ANSYS TurboGrid*. ANSYS, Inc., Canonsburg, PA 15317 USA.

[9] **Gülen, C. S.** (2019). *Gas Turbines for Electric Power Generation* (1st ed.). Cambridge University Press.

[10] **B.Eng., S. D. L., PhD, & Ph.D., H. C.** (2013). *Fluid Mechanics and Thermodynamics of Turbomachinery* (7th ed.). Butterworth-Heinemann.

[11] **Murty, D., V.** (2018). *Turbomachinery: Concepts, Applications, and Design* (1st ed.). CRC Press.

[12] **Wendt, J.** (2008). *Computational Fluid Dynamics*. Springer Publishing.

[13] **Launder, B., & Spalding, D.** (1974). The numerical computation of turbulent flows. *Computer Methods In Applied Mechanics And Engineering, 3*(2), 269-289. https://doi.org/10.1016/0045-7825(74)90029-2

[14] **Suder, K. L.** (1996). *Experimental Investigation of the Flow Field in a Transonic, Axial Flow Compressor with Respect to the Development of Blockage and Loss* [Doctoral dissertation]. https://ntrs.nasa.gov/citations/19970001675

[15] **Piollet, E., Nyssen, F., & Batailly, A.** (2019). Blade/casing rubbing interactions in aircraft engines: Numerical benchmark and design guidelines based on NASA rotor 37. *Journal of Sound and Vibration, 460*, 114878. https://doi.org/10.1016/j.jsv.2019.114878

[16] **Reid, L., & Moore, R. D.** (1978). *Design and overall performance of four highly loaded, high speed inlet stages for an advanced high-pressure-ratio core compressor*. NASA. https://ntrs.nasa.gov/citations/19780025165

[17] **Ahmad, N., Bin, J., Qun, Z., Abdu Ahmad, S., & Fawzy, H.** (2020). Performance Enhancement of a Transonic Axial Flow Compressor with Circumferential Casing Grooves to Improve the Stall Margin. *Journal of Applied Fluid Mechanics, 13*(1), 221–232. https://doi.org/10.29252/jafm.13.01.30147

[18] **Song, L., Guo, Z., Li, J., & Feng, Z.** (2016). Research on Metamodel-Based Global Design Optimization and Data Mining Methods. *Journal of Engineering for Gas Turbines and Power, 138*(9). https://doi.org/10.1115/1.4032653

[19] *RhoSimpleFoam*. (n.d.). OpenFOAMWiki. Retrieved August 10, 2021, from https://openfoamwiki.net/index.php/RhoSimpleFoam

[20] **Dunham, J.** (1998). *CFD Validation for Propulsion System Components*. AGARD Advisory Report 355.

31

6 CURRICULUM VITAE

Name Surname	: Halit OKUMUŞ
Nationality	:Turkey
Date and Place of Birth	:1993, Kahramanmaraş
Language	:English and Turkish
E-Mail	:okumush@itu.edu.tr
Phone	:+905467191414
General Education	:
	B.Sc. 2021, Istanbul Technical University, Faculty of Aeronautics and Astronautics, Aeronautical Engineering
Work Experience	:
	2018, Turkish Airlines, Dir. IT Strategy and Governance